

Dynamics and hysteresis in square lattice artificial spin ice

G. M. Wysin*

Department of Physics, Kansas State University, Manhattan, KS 66506-2601

W. A. Moura-Melo,[†] L. A. S. Mól,[‡] and A. R. Pereira[§]

Departamento de Física, Universidade Federal de Viçosa, 36570-000 - Viçosa - Minas Gerais - Brazil.

(Dated: February 21, 2013)

Dynamical effects under geometrical frustration are considered in a model for artificial spin ice on a square lattice in two dimensions. Each island of the spin ice has a three-component Heisenberg-like dipole moment subject to shape anisotropies that influence its direction. The model has real dynamics, including rotation of the magnetic degrees of freedom, going beyond the Ising-type models of spin ice. The dynamics is studied using a Langevin equation solved via a second order Heun algorithm. Thermodynamic properties such as the specific heat are presented for different couplings. A peak in specific heat is related to a type of melting-like phase transition present in the model. Hysteresis in an applied magnetic field is calculated for model parameters where the system is able to reach thermodynamic equilibrium.

PACS numbers: 75.75.+a, 85.70.Ay, 75.10.Hk, 75.40.Mg

Keywords: magnetism, spin-ice, frustration, magnetic hysteresis, susceptibility.

I. INTRODUCTION: SQUARE SPIN ICE, FRUSTRATION, DYNAMICS

Artificial spin ices are systems in two dimensions that mimic the usual three-dimensional spin ice materials that exhibit geometrical frustration effects: not all the pairwise spin interactions can be satisfied simultaneously^{1–5}. The name spin ice comes from the fact that lowest energy states obey the ice rule. For a square lattice, at each vertex where four spins meet, two point inward while two point outward. Artificial spin ice compounds are built from magnetic nanoislands (typically, permalloy) which can be organized in different geometries where the frustration is manifested^{6–14}.

Here, our focus is on artificial square lattice spin ice, first fashioned and studied by Wang *et al.*⁶ in 2006. Artificial square ice consists of magnetic nanoislands (with a shape that looks like a “cigar”) arranged as shown in Ref.⁶ and here in Fig. 1. Each nanoisland contains a net magnetic moment that tends to point along its long axis. When the interactions between neighboring islands are increased, the system increasingly fills with vertices that obey the two-in/two-out ice rule. Despite this, the predicted ground state of square ice was not observed experimentally until the work by Morgan *et al.*¹⁵ in 2011. Using magnetic force microscopy, those authors observed large regions of their samples which were able to adopt the square ice ground state. Morgan *et al.* also observed the predicted excitations above the ground state, which resemble magnetic monopoles connected by energetic strings^{15–18} (similar to Nambu monopoles¹⁹). These elementary excitations are different from those of natural three-dimensional spin ices, which are magnetic monopoles connected by observable but non-energetic strings^{4,5}. Therefore, these artificial compounds have attracted great interest in recent years.

Thermal activation of the island’s magnetic moment

(spin) configurations is very weak or nonexistent, particularly with square lattice ice. Lack of thermalization is an important topic for experimental artificial spin ices and it can be partially alleviated by applying varying external magnetic fields^{7,20}. Moreover, reductions in island volume and magnetic moment through state-of-the-art nanofabrication can bring energy scales closer to room temperature, leading to thermally driven slow dynamics. Alternatively, the use of materials with an ordering temperature near room temperature seems to be another important possibility. By using such a material, a recent experimental work on a square lattice in an external magnetic field confirms a dynamical “pre-melting” of the artificial spin ice structure at a temperature well below the intrinsic ordering temperature of the island material, creating a spin ice array that has real thermal dynamics of its artificial spins over an extended temperature range²¹. Better understanding of these compounds may even come from colloidal systems, which have an advantage over the usual magnetic arrays because thermal activation of the effective spin degrees of freedom is possible¹¹. So, a more detailed analysis of the effects of thermal fluctuations and the spin dynamics in a two-dimensional spin ice material should be of great interest for a better understanding of these interesting frustrated systems.

Using an Ising model for the magnetic moments of the nanoislands, thermal effects in artificial square ice were studied recently by some of us²² with Monte Carlo simulation. The focus was to examine the roles of elementary excitations in the thermodynamic properties of these systems. We found that the specific heat and average separation between monopoles with opposite charges exhibit a sharp peak and a local maximum, respectively, at the same temperature²², $T_p \approx 7.2D/k_B$, where D is the strength of the dipolar interactions and k_B is Boltzmann’s constant. The Ising behavior of the islands seems to be realistic for the typical artificial magnetic ices made

of permalloy (Py). However, an Ising-type model does not display real time dynamics and it may also incorrectly estimate the degree to which energy barriers in dipolar reversal prevent thermalization. In this article, we study possibilities beyond the Ising behavior for the nanoislands. Our attention shifts to magnetic ices with real dynamics and the extra features that such dynamics may produce. The internal structure and shape of the magnetic nanoislands is taken into account, assuming they are small enough to remain quasi-single-domain during reversal (with nearly coherent dipole rotation).

The theoretical study of the net magnetic moment (with more degrees of freedom) of individual magnetic nanoislands with different sizes and shapes is the initial point. We presented a detailed study of non-Ising behavior for individual islands in Ref.²³, which also verified the coherent rotation of the dipole moment at small island sizes with high aspect ratios. Based on that, we assume that a nanoisland's spin is free to point in any possible direction, but with strong shape anisotropy energies that favor preferred directions. Then, differently from previous articles published on this topic, which consider only the dipolar interactions among the islands, here, these additional anisotropy terms are included in the Hamiltonian. Thus, using a Langevin dynamics approach we have studied different models for possible artificial square spin ices. Our results indicate that systems exhibiting real dynamics are feasible, in such a way that their ground states could be achieved. On the other hand, for ordinary realizations with Py islands the system is not thermally driven to its ground state indicating a possible dynamical bottleneck, absent in systems with real dynamics.

The article is organized as follows: In Section II, the model is explained in detail. We define two order parameters to identify whether the ground state can be accessed at low temperature. Three models (denoted by A,B,C) with different lattice and island parameters are studied to see the possibility of thermalized spin ice dynamics. In Section III, some thermal equilibrium properties of the models A,B,C are calculated. In Section IV, we present some hysteresis calculations and, finally, some discussions and conclusions are given in Section V.

II. THE MODEL SYSTEM

The open square ice system with $N_c = L_1 \times L_2$ unit cells can be set up as follows. One can define the sites of a square lattice in the usual way: the k^{th} lattice site (a monopole charge center or vertex) is at a point $\vec{r}_k = (x_k, y_k)$, where $x_k = m_k a$ and $y_k = n_k a$ are integer multiples of the chosen lattice constant a . The points are chosen to fit inside the desired $L_1 \times L_2$ area. For each unit cell of size $a \times a$ there are two nano-islands that act as a two-atom basis, with the locations,

$$\begin{aligned} \vec{r}_{k1} &= (m_k + \frac{1}{2}, n_k)a, \\ \vec{r}_{k2} &= (m_k, n_k + \frac{1}{2})a, \end{aligned} \quad (1)$$

where the “1” and “2” refer to the sublattices. The nano-island on the 1st sublattice has its long axis in the x direction; the other nano-island, on the 2nd sublattice, has its long axis in the y direction. There are $N = 2N_c$ islands in the whole system.

A 3D vector magnetic moment $\vec{\mu}_i, i = 1, 2, 3 \dots N$ is associated with each island, whose defined center position is some \vec{r}_i . Each \vec{r}_i is selected from the set of $\vec{r}_{k\sigma}$, where $\sigma = 1, 2$ denotes the sublattice. We use indices k, l for locations of the unit cells, and indices i, j for locations of individual islands or their dipoles.

The dipoles are assumed to have fixed magnitude μ , while their direction is represented by a unit vector $\hat{\mu}_i$. The magnetic moments interact via long-range dipole forces, and are also affected by two forms of local shape anisotropy. First, there is a uniaxial anisotropy that impedes free rotation in the xy -plane, associated with some energy constant K_1 , and oriented along x for the first sublattice and along y for the second. Dependent on its sublattice, each moment has an axis \hat{u}_i (equal to \hat{x} or \hat{y}) for this anisotropy, see Fig. 1. Second, because the nano-islands are thin in the z -direction, the z -direction is a hard axis, and there is a hard-axis anisotropy whose energy scale is determined by a constant K_3 , the same for all the islands. The Hamiltonian is then

$$\begin{aligned} \mathcal{H} &= -\frac{\mu_0 \mu^2}{4\pi a^3} \sum_{i>j} \frac{[3(\hat{\mu}_i \cdot \hat{r}_{ij})(\hat{\mu}_j \cdot \hat{r}_{ij}) - \hat{\mu}_i \cdot \hat{\mu}_j]}{(r_{ij}/a)^3} \quad (2) \\ &+ \sum_i \left\{ K_1 [1 - (\hat{\mu}_i \cdot \hat{u}_i)^2] + K_3 (\hat{\mu}_i \cdot \hat{z})^2 - \vec{\mu}_i \cdot \vec{B}_{\text{ext}} \right\} \end{aligned}$$

Here μ_0 is the magnetic permeability of space, and \hat{r}_{ij} is the unit vector pointing from the position of $\vec{\mu}_j$ towards the position of $\vec{\mu}_i$. The first sum is the dipole-dipole interactions, the second sum contains the anisotropy energies and an applied external magnetic induction $\vec{B}_{\text{ext}} = \mu_0 \vec{H}_{\text{ext}}$. A constant is included in the K_1 anisotropy energy so that that energy is zero when a dipole points along its local anisotropy axis \hat{u}_i . Note that if a dipole moves in the xy plane, it only pays the cost of the K_1 anisotropy term, but motion up out of the xy plane (say, in the xz plane) involves an energy proportional to the sum of both anisotropies, $K_1 + K_3$.

The motion out of the xy plane is also impeded by the dipolar interactions. With the dipole pair distances scaled by the lattice constant, the effective strength of nearest neighbor dipolar interactions is determined by the dipole energy factor,

$$D = \frac{\mu_0 \mu^2}{4\pi a^3}. \quad (3)$$

Depending on the island geometry, which is discussed further below, the anisotropy constants K_1 and K_3 would typically be of similar order of magnitude. Thus, there are three important energy scales: dipolar energy, anisotropy energy, and the thermal energy $k_B T$. The anisotropy constants are proportional to the volume V

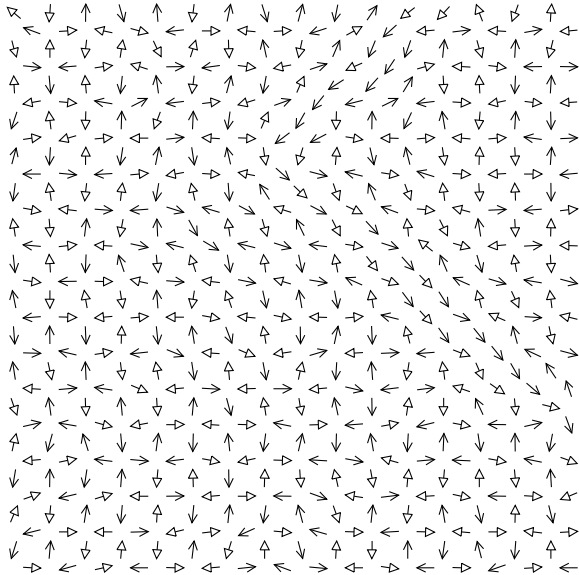


FIG. 1: A 16×16 model system with $d = k_1 = k_3 = 0.1$, in a metastable state at temperature $k_B T/\varepsilon = 0.025$, from a hysteresis scan (this is a state at $h_{\text{ext}} = 0$). Most of the system is locally close to the $Z = +1$ ground state. The upper right hand corner is locally near the $Z = -1$ ground state, and there is a bent domain wall connecting the two regions. For interior charge sites (junction points of four islands), there happens to be no discrete monopole charges present: all $q_k = 0$ and the discrete $\rho_m = 0$.

of the islands, as is $\mu = M_s V$, where M_s is the saturation magnetization of the magnetic material. But then, this dipolar constant D increases as the squared island volume. Thus, changing the island size and spacing a can be used to adjust these energy scales in relation to each other. Typically, the interesting case must have the thermal energy less than both the effective dipolar energy (per site) and anisotropy energy. But note, the effective dipolar energy can be quite a lot larger than that indicated by D , which only measures the energy in a nearest neighbor pair. When the dipolar interactions are summed, the net dipolar energy per island could be much larger than D .

A. Spin-ice ground state and order parameters

For the square lattice spin-ice, the ground state is two-fold degenerate, and involves alternating dipoles on each of the two sublattices. The ground state fully satisfies the two-in/two-out rule in each monopole charge cell (junction of four islands at the site \vec{r}_k of each unit cell). The unit cell positions are expressed $\vec{r}_k = (m_k, n_k)a$, where a is the lattice constant and m_k and n_k are integers. Then one of the ground states can be constructed by setting

the dipole directions as:

$$\begin{aligned}\hat{\mu}_{k1}^{\text{GS}} &\equiv \hat{\mu}_1^{\text{GS}}(\vec{r}_k) = +(-1)^{m_k+n_k} \hat{x}, \\ \hat{\mu}_{k2}^{\text{GS}} &\equiv \hat{\mu}_2^{\text{GS}}(\vec{r}_k) = -(-1)^{m_k+n_k} \hat{y}.\end{aligned}\quad (4)$$

This formula is arranged so that at a chosen unit cell at position \vec{r}_k , the dipole on one sublattice points inward and the dipole on the other sublattice points outward, thereby globally enforcing the two-in/two-out rule. By reversing the sign on all the dipoles, the other ground state is obtained.

With the ground state determined, we can construct a measure of the proximity (in phase space) of any arbitrary state to one of the ground states. This order parameter Z is simply the overlap with this ground state:

$$Z \equiv \langle \psi^{\text{GS}} | \psi \rangle = \frac{1}{2N_c} \sum_{k=1}^{N_c} \sum_{\sigma=1}^2 \hat{\mu}_{k\sigma}^{\text{GS}} \cdot \hat{\mu}_{k\sigma}. \quad (5)$$

The index σ labels the sublattice. If the system happens to be found in the ground state defined in Eq. (4), then $Z = 1$; if the system is in the inverted ground state, then $Z = -1$. Thus it is possible to show that the range of Z is from -1 to +1. This order parameter is useful for indicating the degree of thermodynamic excitation in the system, by the deviation of $|Z|$ from unity. Further, its sign then gives an indication of processes which involve the transformation from one ground state to the other. Indeed, considered even as a local variable (calculating only near a single charge cell), we can track when the system has different regions close to either of the ground states, possibly with regions separated by domain walls. Fig. 1 shows an example, where the system has a region near one of the ground states, with $Z \approx +1$, separated by a domain wall from another region that is near the other ground state, with $Z \approx -1$. The net averaged value of Z for the entire system, however, acquires an intermediate value, $Z \approx 0.521$, indicating considerable separation from a uniform ground state.

The other obvious order parameter to be measured is the areal density of monopole charges, ρ_m . We make a simple discrete definition, to connect to Ising spin ice models, and, a more generalized continuous definition that accounts for the greater freedom of the continuous dipoles in the model described here. The discrete definition of a monopole charge involves counting the net number of dipoles that point outward at a chosen charge site \vec{r}_k , and dividing that result by two. There are four dipoles $\vec{\mu}_{i_k}, i_k = 1, 2, 3, 4$, surrounding any charge cell center \vec{r}_k . Then the possible monopole charge values are $q_k = 0, \pm 1, \pm 2$; the double charges, $q_k = \pm 2$, may typically be of low probability but contribute doubly to the charge density. For the discrete charge definition, whether a dipole points *outward* or *inward* is determined with a Heaviside step function $H(x)$:

$$q_k = \frac{1}{2} \sum_{i_k=1}^4 [2H(\hat{\mu}_{i_k} \cdot \hat{v}_{i_k}) - 1]. \quad (6)$$

The unit vectors $\hat{v}_{i_k}, i_k = 1, 2, 3, 4$, point outward from charge site \vec{r}_k to each of the four nearest islands.

Because this discrete definition can show sudden change when a dipole rotates 90° from the radially outward direction, we also considered a continuous definition. In the continuous definition, the step function is removed, and only a scalar product is needed,

$$q_k = \frac{1}{2} \sum_{i_k=1}^4 \hat{\mu}_{i_k} \cdot \hat{v}_{i_k}. \quad (7)$$

In contrast to the discrete definition, this charge definition varies continuously from $q_k = -2$ to $q_k = +2$. One can also note that for either the discrete or the continuous definition, total monopole charge is conserved. A positive contribution produced by some dipole at one charge cell is accompanied by an equal negative contribution at a neighboring charge cell (each dipole contributes to two charge cells). Then, the total algebraic monopole charge in the system takes the conserved value, zero.

In order to get a measure of the monopole charges present, regardless of their sign, we define a density for the system as a whole, by applying absolute value. Thus, the ‘‘monopole density’’ measured in the simulations here is defined as

$$\rho_m = \langle |q_k| \rangle = \frac{1}{N_c} \sum_{k=1}^{N_c} |q_k| \quad (8)$$

This is averaged over charge cells. By using absolute value, the definition does not allow the cancellation of charges of opposite signs. Note that in either of the ground states, there are no charges at any sites, and $\rho_m = 0$. Charges appear as the system moves away from the ground state. (This is true for the spin ice on the square lattice, but not on the Kagomé lattice, whose ground state contains charges, due to there being three dipoles for each charge cell.) Thus, this is another measure of excitation in the system.

At very high temperature, the individual dipoles can point freely in all directions. In this high-entropy limit, the value of ρ_m from both definitions can be determined. For the discrete definition, each of the four dipoles in a vertex are in or out with equal probabilities. Of the 16 possible states, there are 6 with $q_k = 0$, 8 with $q_k = \pm 1$ and 2 with $q_k = \pm 2$. The average charge per vertex, including single and double charges, is

$$\rho_m = \langle |q_k| \rangle = (6 \times 0 + 8 \times 1 + 2 \times 2)/16 = 3/4. \quad (9)$$

For the continuous definition, there is a corresponding expression from averaging over the sum of projections $x_{i_k} \equiv \hat{\mu}_{i_k} \cdot \hat{v}_{i_k}$ of dipoles on their local axes, see (7). With each x_{i_k} ranging from -1 to $+1$, we have the average in an arbitrary cell

$$\rho_m = \frac{\int dx_1 dx_2 dx_3 dx_4 \frac{1}{2} |x_1 + x_2 + x_3 + x_4|}{\int dx_1 dx_2 dx_3 dx_4 1} = 7/15. \quad (10)$$

We note that while these should be the limits in the state of greatest disorder, they are not upper limits. One can observe that, for example, by taking the ground state configuration and reversing the dipoles only on one sublattice, a state will be obtained that has a doubly-charged monopole in every cell. That state would have $\rho_m = 2$ by both definitions. Thus, the whole range $0 \leq \rho_m \leq 2$ is allowed.

B. The undamped dynamics

The zero-temperature, undamped dynamics of each magnetic dipole is determined by a torque equation,

$$\frac{d\vec{\mu}_i}{dt} = \gamma \vec{\mu}_i \times \vec{B}_i \quad (11)$$

where \vec{B}_i is the local magnetic induction acting on the i^{th} dipole, and γ is the electronic gyromagnetic ratio. The local magnetic induction is derived from the Hamiltonian by assuming an energy $-\vec{\mu}_i \cdot \vec{B}_i$ for each dipole, i.e.,

$$\begin{aligned} \vec{B}_i = & -\frac{\delta \mathcal{H}}{\delta \vec{\mu}_i} = -\frac{1}{\mu} \frac{\delta \mathcal{H}}{\delta \hat{\mu}_i} = \frac{D}{\mu} \sum_{j \neq i} \frac{3(\hat{\mu}_j \cdot \hat{r}_{ij}) \hat{r}_{ij} - \hat{\mu}_j}{(r_{ij}/a)^3} \\ & + 2 \frac{K_1}{\mu} (\hat{\mu}_i \cdot \hat{u}_i) \hat{u}_i - 2 \frac{K_3}{\mu} (\hat{\mu}_i \cdot \hat{z}) \hat{z} + \vec{B}_{\text{ext}}. \end{aligned} \quad (12)$$

It will be convenient to choose some standard units for the time, the applied field, and so on, to simplify and scale the numerical calculations. The dipole terms are simplified by selection of the lattice constant a as the unit of length. A natural unit to measure field \vec{H}_{ext} is the saturation magnetization M_s from which the particles are made. For example, for permalloy, with $M_s = 860$ kA/m, this unit as a magnetic induction is close to one tesla: $\mu_0 M_s \approx 1.08$ T. Using this quantity to scale the magnetic field and hence the magnetic induction defines their dimensionless field,

$$\vec{h}_{\text{ext}} = \frac{\vec{H}_{\text{ext}}}{M_s} = \frac{\vec{B}_{\text{ext}}}{\mu_0 M_s}. \quad (13)$$

When \vec{h}_{ext} approaches 1.0 the applied field should have a strong tendency to saturate the magnetization of the system (if the dipolar interactions do not impede that). This then indicates how to scale the dipole and anisotropy fields, i.e., by writing the dimensionless local magnetic fields from (12),

$$\begin{aligned} \vec{h}_i = & \frac{\vec{B}_i}{\mu_0 M_s} = \frac{D}{\mu \mu_0 M_s} \sum_{j \neq i} \frac{3(\hat{\mu}_j \cdot \hat{r}_{ij}) \hat{r}_{ij} - \hat{\mu}_j}{(r_{ij}/a)^3} \\ & + 2 \frac{K_1}{\mu \mu_0 M_s} (\hat{\mu}_i \cdot \hat{u}_i) \hat{u}_i - 2 \frac{K_3}{\mu \mu_0 M_s} (\hat{\mu}_i \cdot \hat{z}) \hat{z} + \vec{h}_{\text{ext}}. \end{aligned} \quad (14)$$

This involves dimensionless coupling constants that indicate the relative strength of each contribution,

$$d = \frac{D}{\mu\mu_0 M_s} = \frac{\mu}{4\pi a^3 M_s}, \quad (15)$$

$$k_1 = \frac{K_1}{\mu\mu_0 M_s}, \quad k_3 = \frac{K_3}{\mu\mu_0 M_s}. \quad (16)$$

These definitions involve the different energy scales divided by an energy unit,

$$\varepsilon \equiv \mu_0 \mu M_s, \quad (17)$$

that depends on the size of the magnetic islands. The dimensionless dipole parameter d can be seen to be proportional to the volume fraction of the system occupied by magnetic islands, since $\mu = M_s V$ for each island. Obviously a higher packing of magnetic material into the lattice leads to stronger dipolar effects, and d indicates their effective strength.

The dynamic equation can be scaled in the same way, so that the dimensionless field appears on the RHS. Then the dynamics for the unit vector dipoles is described using a rescaled time τ ,

$$\frac{d\hat{\mu}_i}{d\tau} = \hat{\mu}_i \times \vec{h}_i, \quad \tau = \gamma\mu_0 M_s t. \quad (18)$$

With the above scaling of the fields, the unit of time is $(\gamma\mu_0 M_s)^{-1}$. For the case of permalloy and using the gyromagnetic ratio as $\gamma = e/m_e \approx 1.76 \times 10^{11} \text{ T}^{-1} \text{ s}^{-1}$, this unit is $(\gamma\mu_0 M_s)^{-1} \approx 5.26 \text{ ps}$.

C. Island geometry and energetics

The shape anisotropy constants K_1 and K_3 can be estimated based on the magnetic properties for permalloy (or other material) and micromagnetics simulations for the choice of island geometries and island volume V . We consider thin elliptical islands. Here L_x denotes the major-diameter of the ellipse and L_y is the minor-diameter, while L_z is the height of the island or its thickness. The semi-major axis is $A = L_x/2$, the semi-minor axis is $B = L_y/2$. It is well-known that an elliptically shaped magnetic particle will have anisotropy²⁴ within the plane of the island. In Ref.²³, the anisotropy constants (as energies per unit volume) were estimated based on a calculational approach for thin elliptical islands, for a range of thicknesses $L_z \ll L_x$, characterized by an aspect ratio $g_3 = L_x/L_z$, and various lateral aspects ratio $g_1 = L_x/L_y$. Here we consider some different sizes and shapes for the islands and discuss the expectations for their dynamics and the relative importance of the different energy scales when placed in a square spin-ice array.

Model A. In Wang *et al.*⁶, experiments on square spin-ice were carried out for (quasi-rectangular) particles with dimensions $220 \text{ nm} \times 80 \text{ nm} \times 25 \text{ nm}$, where the last number is the vertical thickness. In those experiments, the particle sizes were kept fixed, but different

lattice parameters a from 320 nm to 880 nm were used. In this first model, we use these numbers to describe elliptical particles: $L_x = 220 \text{ nm}$, $L_y = 80 \text{ nm}$, $L_z = 25 \text{ nm}$. Then the particle volume is $V = \pi A B L_z = 3.46 \times 10^5 \text{ nm}^3$, and using a saturation magnetization $M_s = 860 \text{ kA/m}$ for Py, the magnetic dipole moment per particle is $\mu = 2.97 \times 10^{-16} \text{ A}\cdot\text{m}^2$, the equivalent of about 3.2×10^7 Bohr magneton. For its aspect ratio parameters $g_1 = 2.75$ and $g_3 = 8.8$, the anisotropy energy densities can be found by interpolation of the simulation results in Ref.²³, as $K_1/V = 0.0064 \text{ A}_{\text{ex}}/\text{nm}^2$ and $K_3/V = 0.0143 \text{ A}_{\text{ex}}/\text{nm}^2$, where $A_{\text{ex}} \approx 13 \text{ pJ/m}$ is the exchange stiffness for Py. The easy-axis anisotropy is then $K_1 = 2.9 \times 10^{-17} \text{ joules}$, while the hard-axis anisotropy is estimated as $K_3 = 6.4 \times 10^{-17} \text{ J}$. These are considerably larger than room-temperature (300 K) thermal energy $k_B T \approx 4.1 \times 10^{-21} \text{ J}$, as needed for stable magnetic moments. The energy unit is $\varepsilon = \mu_0 \mu M_s = 3.21 \times 10^{-16} \text{ J}$. Then the dimensionless anisotropies are $k_1 = K_1/\varepsilon = 0.0897$, $k_3 = K_3/\varepsilon = 0.200$. The scaled thermal energy at room temperature is $\mathcal{T} \equiv k_B T/\varepsilon = 1.29 \times 10^{-5}$, an extremely small value.

The nearest neighbor dipolar energy scale might be estimated first at lattice constant $a = 880 \text{ nm}$, for which it is $D = 1.29 \times 10^{-20} \text{ J}$, about 2000 times smaller than K_1 . If instead the lattice constant $a = 320 \text{ nm}$ is used, this will scale up by a factor of $(880/320)^3$, leading to $D = 2.68 \times 10^{-19} \text{ J}$, or still 100 times smaller than K_1 . The dimensionless dipolar coupling for $a = 320 \text{ nm}$ is $d = D/\varepsilon = 8.35 \times 10^{-4}$. Obviously, values of k_1, k_3 , and d similar to these are needed to get a spin-ice system, however, dynamics simulations are difficult with these parameters because the anisotropy is so dominant and Ising-like. Over the time scales that can be accessed in numerical simulations, one would not expect to see much dynamical flipping of the island dipoles, except in the presence of a strong applied magnetic field. Thus it may be interesting instead to consider some other particle sizes where the dynamics can be expected to be more active.

A thinner or smaller island will result in a smaller magnetic dipole moment μ , which leads linearly to weaker anisotropy, but quadratically to weaker dipolar energy. Both energy scales become closer to the thermal energy. Thus we can try to change the particle size in such a way so that room temperature thermal energy is closer to K_1 and perhaps even larger than D .

Model B. Here we consider smaller particles, with $L_x = 40 \text{ nm}$, $L_y = 8.0 \text{ nm}$, $L_z = 4.0 \text{ nm}$, to try and get weaker anisotropy energy scales (for Py parameters). The particle volume is now only $V = 1005 \text{ nm}^3$, and the dipole moment is $\mu = 8.64 \times 10^{-19} \text{ A}\cdot\text{m}^2$. At aspect ratio parameters $g_1 = 5.0$, $g_3 = 10$, the anisotropy energies are found to be somewhat smaller: $K_1 = 1.38 \times 10^{-19} \text{ J}$, and $K_3 = 1.12 \times 10^{-19} \text{ J}$. The energy unit, though, is now also smaller: $\varepsilon = 9.34 \times 10^{-19} \text{ J}$, leading to dimensionless couplings $k_1 = 0.148$ and $k_3 = 0.120$. The smaller energy unit means that room temperature effects

may be more accessible. The scaled thermal energy at 300 K is increased: $\mathcal{T} = k_B T / \varepsilon = 0.00443$. For a lattice with $a = 80$ nm, we find $D = 1.46 \times 10^{-22}$ J, and $d = D / \varepsilon = 1.56 \times 10^{-4}$.

It is clear in the above examples that the strong Ising-like anisotropy for real spin-ice particles dominates over thermal energy at (and below) room temperature. That being the case, we find it interesting also to study a model with fictitious parameters, which might be possible to achieve in other materials with different values of M_s , K_1/V , etc.

Model C. Rather than assuming a particular particle size and using Py parameters, suppose some particles are arranged so that $D = K_1 = K_3 = \frac{1}{10}\varepsilon$. Obviously nature may not easily produce such a system with all equal energy scales, but it may be possible by appropriate materials engineering. We use a fraction of ε , which is required by the definition of d , see Eq. (15) (the volume fraction of dipoles on the lattice cannot be more than unity). The scaled energy parameters are all equal: $d = k_1 = k_3 = 0.1$. A physical value of ε is needed, based on values of μ and M_s for some real particles, to locate room temperature on the temperature scale.

III. THERMAL EQUILIBRIUM PROPERTIES

Mostly the magnetic properties of spin-ice materials are investigated in an approximation of zero temperature, because the fundamental interaction strengths of the anisotropy energies and the dipolar energies are much greater than $k_B T$ at room temperature (Models A & B). Even so, there could be energetic thermal fluctuations in a magnetic system even at low temperatures, in any situation where the magnetic fluctuations are large, such as near a reversal point in a hysteresis loop. This might lead to enhancement of specific heat in such a situation, and of course, thermal rounding of the reversal paths in magnetization hysteresis loops. Thus it could be interesting to have some calculations of the energy, specific heat, and also of magnetic susceptibilities in a situation of thermal equilibrium.

The time evolution from Langevin dynamics can be used to get thermal averages, as an alternative to Monte Carlo calculations, that includes true dynamical effects. Details of the Langevin simulation method, as solved using a second order Heun integrator, with FFT for calculation of the dipole fields, are given in the Appendices. Provided the simulation time is long compared to any physical relaxation time, a sequence of energy samples E_n and total system magnetization samples \vec{M}_n can be averaged, and their fluctuations can be used to estimate the specific heat and magnetic susceptibility. Suppose there are N_s samples taken from the time evolution. The average energy for all N islands is estimated as

$$\langle E \rangle = \frac{1}{N_s} \sum_n E_n \quad (19)$$

with a measurement error estimated from its standard deviation σ_E and the number of samples,

$$\Delta E = \frac{\sigma_E}{\sqrt{N_s}}, \quad \sigma_E^2 = \langle E^2 \rangle - \langle E \rangle^2. \quad (20)$$

The total heat capacity of the system is determined from the fluctuations in the energy,

$$C_N = \beta^2 \langle (E - \langle E \rangle)^2 \rangle = \beta^2 \sigma_E^2, \quad (21)$$

where $\beta = (k_B T)^{-1}$, and from that we obtain the specific heat per island, $C = C_N / N$. The error in the heat capacity is calculated by finding the standard deviation of the quantity $z \equiv (E - \langle E \rangle)^2$ from which C_N was obtained, which is found from the following averages,

$$\sigma_z^2 = \langle E^4 \rangle - \langle E^2 \rangle^2 + 4 \langle E \rangle [2 \langle E^2 \rangle \langle E \rangle - \langle E^3 \rangle - \langle E \rangle^3]. \quad (22)$$

Then the error in C_N is

$$\Delta C_N = \beta^2 \frac{\sigma_z}{\sqrt{N_s}}, \quad (23)$$

and the error in specific heat per island is $\Delta C = \Delta C_N / N$. Likewise, the susceptibility per island, χ_{xx} , is found from fluctuations in total magnetic moment of the system, $M_x = \sum_l \mu_l^x$,

$$\chi_{xx} = \frac{\beta}{N} \langle (M_x - \langle M_x \rangle)^2 \rangle = \frac{\beta}{N} \sigma_{M_x}^2, \quad (24)$$

and its error $\Delta \chi_{xx}$ comes from relations similar to (22) and (23).

Due to the fluctuations caused by the temperature in the simulations, the calculations of C and χ are generally not as precise as those of $\langle E \rangle$ and $\langle \vec{M} \rangle$, without making very long runs. Especially as mentioned above, these calculations are difficult in any physical situation where the magnetization is on the verge of reversal, where the fluctuations are greatest.

The system was started in a random state, with the temperature initially set at the highest value in the range of interest. For a chosen temperature, data samples were taken at some appropriate time interval that depends somewhat on the energy couplings. For coupling parameters k_1, k_3 on the order of 0.2 or less, and d several orders smaller (Models A & B), a Heun time step $\Delta\tau = 0.01$ was sufficient to insure proper energy conservation at zero temperature. Using this time step for finite temperature together with damping $\alpha = 0.1$, we averaged over $N_s = 4000$ data samples separated by sampling time interval $\Delta\tau_s = 10^3 \Delta\tau = 10.0$. An initial time interval corresponding to 100 samples was allowed for relaxation before samples were taken. Simulations would be left to run even longer than 4000 samples, if necessary, until the percent error in the magnitude of the total system magnetization was found to be less than 0.1%. The final state at one temperature was then used as the initial state for the next lower temperature in the calculation.

For model C, the dipolar coupling is much stronger, and this requires a smaller Heun time step, $\Delta\tau = 0.001$, to insure proper dynamics at finite temperature and energy conservation at zero temperature. Besides this, the calculation parameters for averages were the same as for models A & B, e.g., $N_s = 4000$ and taking samples at sampling time interval $\Delta\tau_s = 10^3\Delta\tau$, while waiting for 0.1% or better precision in the system magnetization.

Some thermodynamic results for the Wang *et al.* particles (Model A) are shown in Fig. 2, versus scaled temperature $\mathcal{T} = k_B T / \epsilon$. A 16×16 grid of cells was used ($N = 2 \times 16^2 = 512$). As the dimensionless energy coupling constants are small numbers, the only interesting effects are observed for $\mathcal{T} < 0.1$. Near $\mathcal{T} \approx 0.02$ there are peaks in specific heat and in the in-plane components of magnetic susceptibility. As mentioned earlier, though, these features would appear only greatly above room temperature, which is marked with arrows. At these “high” temperatures, other modifications would take place first (besides magnetic effects) and the model would not be applicable. Note that the monopole charge density in Fig. 2c does not go to zero at very low temperature here. It does, however, make a transition to a lower value. This is an indication that the system did not find a state close to a ground state. There is frozen-in disorder at lower temperatures. It is also an indication that the time scale for thermal relaxation to an equilibrium configuration was longer than the time interval used for averaging. However, the specific heat per site does tend towards $C/k_B \rightarrow 1$ as $T \rightarrow 0$, consistent with the dipoles simply making small fluctuations around their local anisotropy axes (the long axes of the islands). In contrast to this, an Ising model for this system would lead to C/k tending towards zero for low temperature. Both the discrete and continuous definitions of ρ_m exhibit similar behaviors, and they tend towards the expected high-temperature limits of $3/4$ and $7/15$, respectively. At very low temperatures they trend together and give a nearly identical limit as $T \rightarrow 0$. The order parameter Z (not shown) stayed close to zero for the whole temperature range shown. That is further indication of the system staying far from a ground state, where it would have reached one of the values ± 1 . The dipoles in this limit are nearly aligned with the islands’ long axes, however, with a frozen-in disorder, not near a ground state.

Results for Model B’s smaller particles are shown in Figure 3. These confirm that for the typical square lattice spin-ice using Py as the material, the room-temperature thermodynamics is nearly the same as that at zero temperature. There would be some limiting specific heat $C \approx k_B$ and non-zero value for the in-plane susceptibility. However, the monopole density has extreme difficulty to go to zero while scanning from high to low temperature, although both the discrete and continuous definitions tend to the same value at very low temperature. Then, in fact, the dynamics is a low temperature dynamics in a disordered non-ground state (and non-equilibrium) configuration.

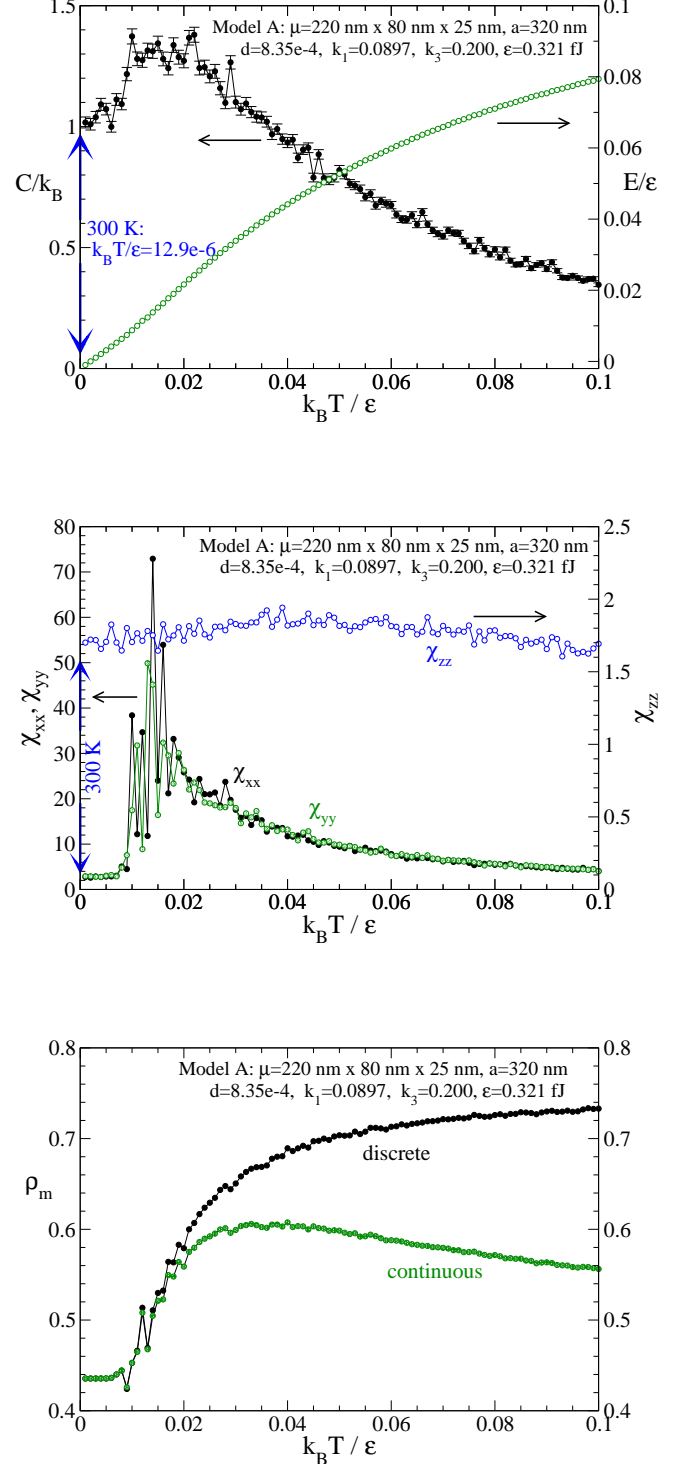


FIG. 2: (Model A) For a 16×16 grid of particles as used in Wang *et al.* with indicated parameters, (a) the internal energy and specific heat per site versus scaled temperature; (b) the components of the magnetic susceptibility at zero external field; (c) The monopole density, Eq. (8) as determined from discrete and continuous charge definitions, Eqs. (6) and (7). The vertical arrows very near $k_B T / \epsilon = 0$ show room temperature: it is essentially inaccessible in this dynamics.

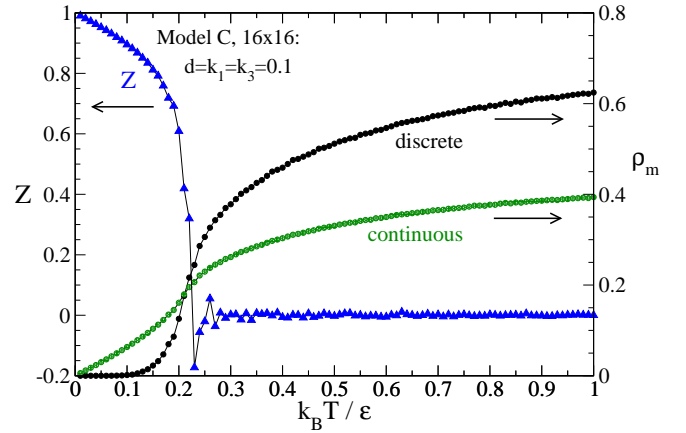
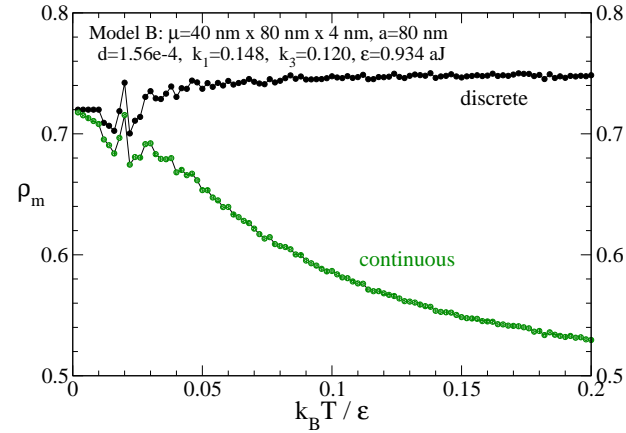
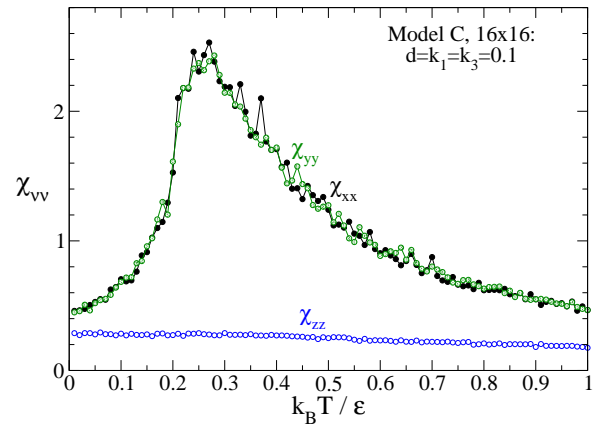
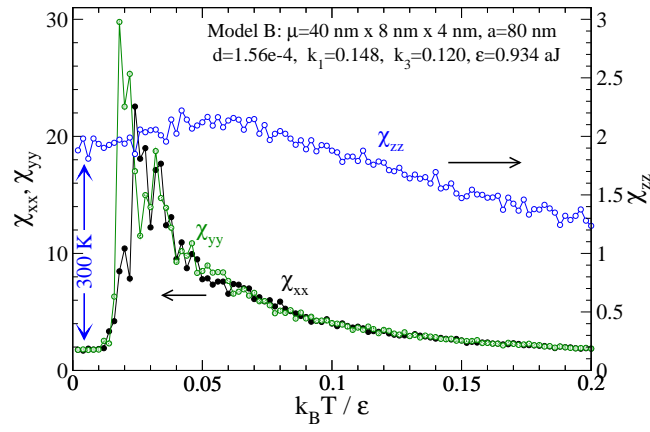
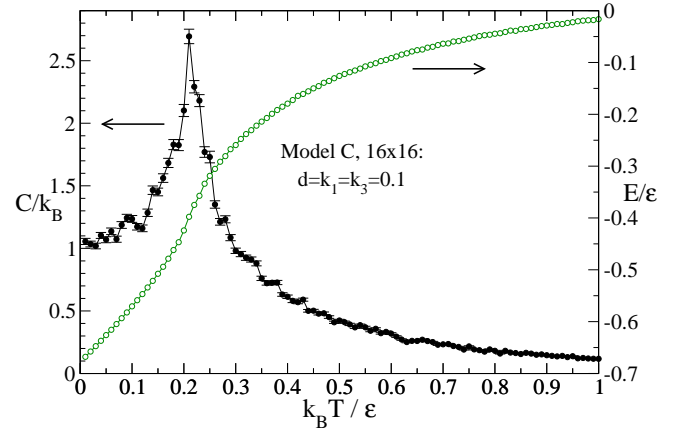
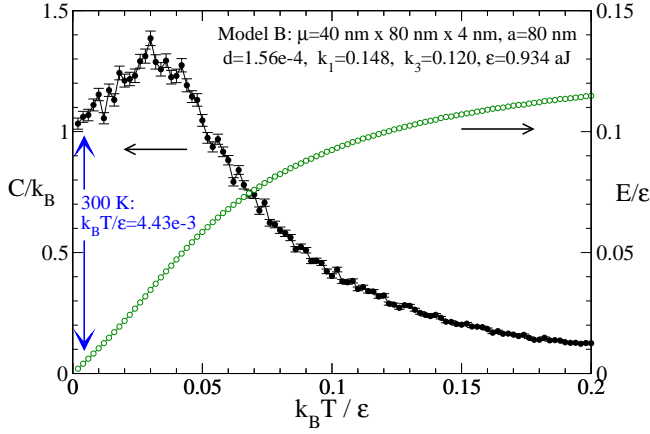


FIG. 3: (Model B) For a 16×16 grid of still smaller sized particles with indicated parameters and an even lower energy scale, (a) the average internal energy per site and the specific heat per site versus scaled temperature; (b) the components of the magnetic susceptibility at zero external field; (c) the monopole charge density.

FIG. 4: (Model C) For the model with $D = K_1 = K_3 = \frac{1}{10}\epsilon$, (a) the average internal energy per site (in energy units ϵ) and the resulting specific heat per site versus scaled temperature; (b) the components of the magnetic susceptibility at zero external field; (c) the monopole charge density together with the ground state overlap order parameter Z .

The thermodynamic results for 16×16 theoretical Model C are shown in Figure 4. There is a strong peak in specific heat near $\mathcal{T} \approx 0.22$ and a more rounded peak in $\chi_{xx} \approx \chi_{yy}$ at a slightly higher temperature. For all of the models studied, the out-of-plane magnetic susceptibility χ_{zz} is considerably smaller than χ_{xx} , and there is only a weak temperature dependence. Notably, Model C does reach thermodynamic equilibrium in the simulations. This is seen clearly in the plots of the order parameters Z and ρ_m . Now ρ_m , for both discrete and continuous forms, tends towards zero at low temperature, as expected for the system moving towards a ground state. Further, the ground state overlap order parameter, Z , tends to go towards unity as $T \rightarrow 0$; this is the strongest indication of approaching one of the ground states. It is by chance that the system ended in $Z = +1$; it could have reached $Z = -1$ with the same probability. At higher temperatures above the peaks in C and χ we see that Z becomes quite close to zero; the system is more random and far from a ground state. In the same high-temperature region, the monopole density tends towards the limiting values, $3/4$ for the discrete formula and $7/15$ for the continuous definition. The discrete definition for ρ_m necessarily undergoes a stronger change in value as the system makes a transition from its low to high temperature behavior. On the other hand, the larger value for the continuous definition at low T gives an indication of the fluctuations of island dipoles around their long axes as $T \rightarrow 0$.

IV. HYSTERESIS CALCULATIONS

A simple experiment to investigate the magnetic properties of spin ice is the response in an applied external field (hysteresis calculation). To get a general impression of the physical response in any square spin ice, hysteresis calculations were carried out for Model C at fixed scaled temperature $\mathcal{T} = 0.1$. These were calculated the same as for the thermodynamics, except that it was adequate to average over shorter sequences, $N_s = 1000$, at each step of the applied field. The system was initially set in a random configuration, but with the maximum positive applied field. The field was scanned to lower and negative values along some axis (either \hat{x} or at 45° to $+\hat{x}$) and then allowed to come back to the starting value. In order to interpret the results, it was also important to calculate the order parameter Z and the monopole charge density ρ_m during the hysteresis scan.

The results for field applied along the \hat{x} axis are shown in Figures 5 and 6. In fact, at this temperature, the model does not exhibit any hysteresis: the magnetization per island is the same in backward and forward scans of \vec{h}_{ext} . However, the magnetization shows regions with distinctly different slopes. In Fig. 5b, one sees that the order parameter Z , however, tends to take on either values close to zero, at strong applied field, or, values near $Z \approx \pm 1$, at weaker field. We note that this temperature

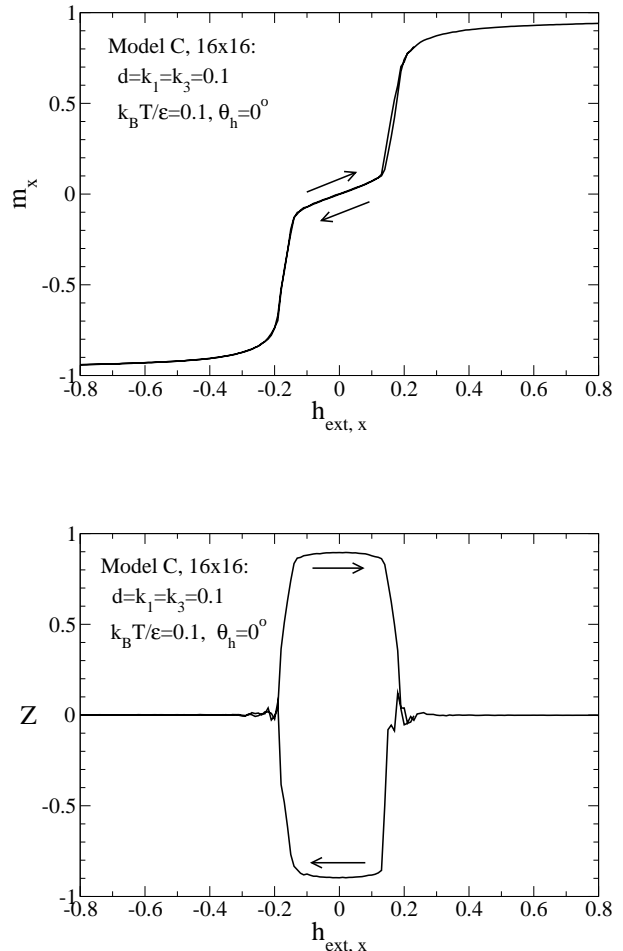


FIG. 5: (Model C) With $D = L_1 = K_3 = \frac{1}{10}\epsilon$, at temperature $k_B T = \frac{1}{10}\epsilon$, (a) the averaged magnetization per site versus external magnetic field h_{ext} applied along the x -axis; (b) the order parameter Z versus h_{ext} . The field strength was initially set at $h_{\text{ext}} = 0.8$, and scanned to $h_{\text{ext}} = -0.8$, then back to the starting value as in a hysteresis loop calculation.

$\mathcal{T} = 0.1$ is on the low side of the specific heat peak for zero magnetic field. Then this shows that in the central region of the MH graph, the system falls into states that are close to the ground states. These states, however, are slightly modified due to tilting of some of the dipoles according to the field strength. Hence, there is close to a linear response with h_{ext} , as the dipoles on the 2nd sublattice, which are nearly perpendicular to the field, get tilted by it.

By chance, the system in Fig. 5 chose $Z = -1$ on the forward scan and $Z = +1$ on the reverse scan. These two states are transformed from one into the other simply by reversing the choice of the 1 and 2 sublattices. Thus, there is no breaking of this symmetry caused by the applied field. There is nothing to prevent both forward and reverse scans from falling into the same state of Z .

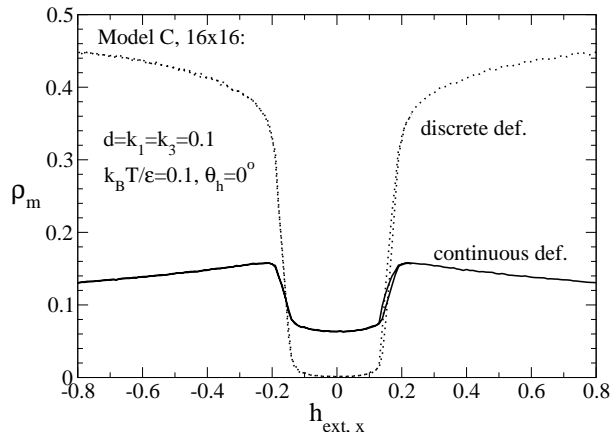


FIG. 6: (Model C) With $D = K_1 = K_3 = \frac{1}{10}\varepsilon$, at temperature $k_B T = \frac{1}{10}\varepsilon$, the averaged monopole density versus external magnetic field h_{ext} applied along the x -axis, for the calculations in Fig. 5. The results of both the discrete and continuous charge definitions are compared here.

The variation of monopole charge density with applied field, for the simulation in Fig. 5, is shown in Fig. 6. Both the discrete and continuous definitions are displayed. The discrete definition has more dramatic changes. Especially, ρ_m tends to zero (or a small value for the continuous version) over the same applied field range where $Z \approx \pm 1$. This confirms clearly that the central region of the MH graph corresponds to the system being in states close to the ground states.

For applied field along an axis at 45° to the $+\hat{x}$ -axis, the situation is similar, see Figures 7 and 8. The MH and ZH graphs are nearly the same as for those for applied field along \hat{x} . In this case, however, the applied field must be causing both sublattice dipoles to tilt at stronger fields. There is a difference, then, in the charge density plot, see Figure 8. Again, in the central region near weak h_{ext} , the monopole density tends to zero, as expected for the system being close to one of the ground states. At strong field, however, the discrete charge density also tends towards zero (as does Z). As the dipoles all tend to align at 45° to $\pm\hat{x}$, the net number of dipoles pointing into any charge site is then forced to be zero. This clearly forces the monopole density found by the discrete definition to zero. One sees that the monopole density by the continuous definition, on the other hand, does not fall to zero at high field, and instead behaves the same as it does for field applied along \hat{x} .

V. DISCUSSION AND CONCLUSIONS

We have studied the possibilities of spin dynamics in frustrated artificial spin ice systems consisting of two-dimensional square lattices of elongated magnetic nanois-

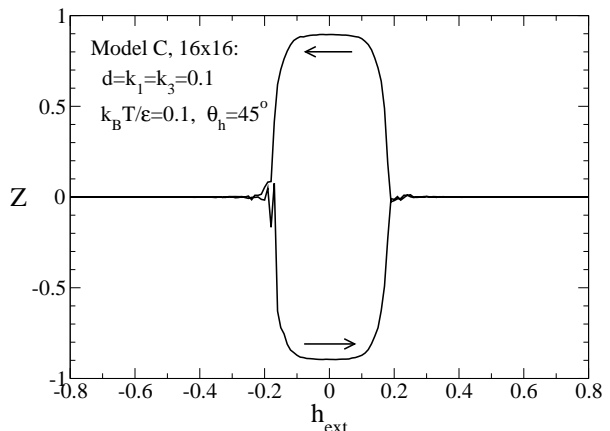
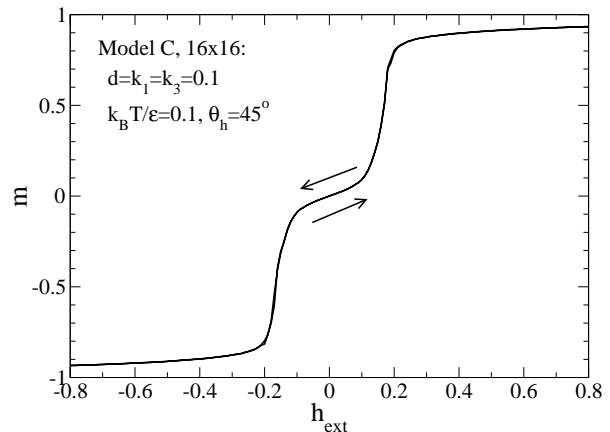


FIG. 7: (Model C) With $D = K_1 = K_3 = \frac{1}{10}\varepsilon$, at temperature $k_B T = \frac{1}{10}\varepsilon$, (a) the averaged magnetization per site versus external magnetic field h_{ext} applied at 45° above the x -axis; (b) the order parameter Z versus h_{ext} . The field strength was initially set at $h_{\text{ext}} = 0.8$, and scanned to $h_{\text{ext}} = -0.8$, then back to the starting value as in a hysteresis loop calculation.

lands. The internal structure of the magnetic nanoislands was taken into account by assuming quasi-single-domain structure. Then, depending on the island shapes, aspect ratios, sizes, elements and organization in the array, we have looked for possible departures from the usual Ising-like behavior. We have found that the systems without real dynamics (islands practically with an effective Ising behavior) have great difficulty to achieve the ground state (models A & B). The order parameter Z (defined in Section II) never reaches the values -1 or $+1$ (the two degenerate ground states), even for very low temperatures. This result agrees with all experimental studies^{6,15} concerning square spin ice. On the other hand, by considering fictitious material constants D , K_1 and K_3 , we found interesting deviations from Ising behavior and consequently, more easily thermalized spin dynamics within

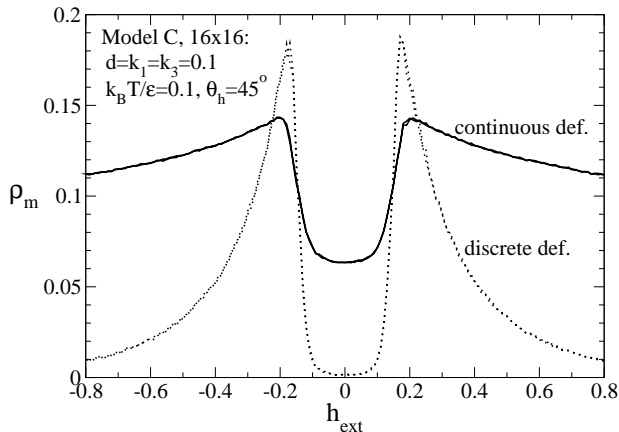


FIG. 8: (Model C) With $D = K_1 = K_3 = \frac{1}{10}\varepsilon$, at temperature $k_B T = \frac{1}{10}\varepsilon$, the averaged monopole density versus external magnetic field h_{ext} applied at 45° above the x -axis, for the calculations in Fig. 7.

the array. For this type of system (model C), the ground state can be easily obtained for low temperatures.

Some of the results obtained here can be directly compared to those of Ref.²², where the artificial square spin ice with point-like dipoles with Ising-like behavior was studied by using conventional Monte Carlo simulations. This model with point-like Ising dipoles will be referred to as model I (see, for instance, Refs.^{16–18,22}). Its ground state ($Z = \pm 1$) for square lattice ice appears naturally for very low temperatures, i.e., by using conventional Monte Carlo simulations. However, our results for models A & B, obtained from Langevin dynamics, showed that the ground state does not appear at low temperatures. This may indicate that there is a kind of dynamic constraint (effectively, excessively long relaxation time) that prevents it from reaching the ground state over a moderate time of observation. Indeed, a similar result is found when the dynamics of the model I in the presence of external magnetic fields is considered^{12,25–28}. This may indicate that artificial square spin ices made with permalloy may never reach the ground state, since both external field dynamics and thermally driven dynamics have bottlenecks that prevent access to the ground state. On the other hand, our results for model C, for materials with fictitious constants, indicate that it may be possible to access the ground state using another kind of material. By changing the island’s anisotropies and interactions, the dynamical bottleneck can be eliminated.

This difference may be associated with the way that the system explores the phase space. First, consider Ising-like islands. Since we are dealing with classical particles, each island must pass through an energy barrier to change its magnetization direction, either by the creation and propagation of a domain wall or by rotation of a single domain. Either way, there is no option for tunneling

and some energy must flow to the island. This internal energy barrier was not taken into account in the Monte Carlo calculations of Refs.^{16,17,22} and probably this is why the ground state was obtained. The results of the present study and those from Refs.^{12,25–27} include the energy barrier for spin flips and we may expect that the existence of a huge energy barrier is responsible for the difficulty to access the ground state. Moreover, in model C, where the energy barrier is smaller, the ground state is accessible. The key factor blocking access to the ground state of artificial square spin ice is the energy barrier for spin flips.

For model I, the specific heat exhibits a peak at a temperature around $7.2D/k_B$, where it is suspected that the string connecting the Nambu monopoles is broken and the system is able to support free monopoles²². The specific heat for models A, B & C also exhibits a characteristic peak. For models A & B, the peak appears for temperatures around $20D/k_B$. However, this value is determined more so by the anisotropy K_1 and not by D . Nonetheless, the ground state cannot be obtained for models A & B even for zero temperature and, therefore, there is not a clear way of establishing equivalences between the results of these models and results of model I. Even so, the peak in the specific heat for model C occurs at a temperature around $2D/k_B$, about three times smaller than in model I. This is expected because there are more spin degrees of freedom for model C than for model I. Furthermore, the specific heat peak moves to higher temperature with increasing K_3 , as expected from the greater restriction of out-of-plane motion it causes.

To complete this study, we also calculated the hysteresis for the model that exhibits dynamics. It is an important calculation to get a general impression of the physical response to an applied external field; the system tends to pass close to a ground state, as indicated by $Z \approx 0$ near the center of the MH loop.

The investigations developed here could help experimental advances toward spin ice systems in which the ground state could be achieved and/or the transition rendered by appearance of free monopoles occurs around room temperature. Experimentally, a recent work was already addressed in this direction. Indeed, Kapaklis *et al.*²¹ have proposed an experimental system (in an external magnetic field) where thermal dynamics can be introduced by varying the temperature of the array. On a square lattice, they use a material (based on δ -doped $Pd(Fe)$) with an ordering temperature near room temperature to confirm a dynamical “pre-melting” of the artificial spin ice structure at a temperature well below the intrinsic ordering temperature of the island material. Such a procedure is capable of creating a spin ice array that has real thermal dynamics of the artificial spins over an extended temperature range²¹. The possibility of observing emergent monopoles is therefore conceivable, following the general approach that the authors of Ref.²¹ described in the design of spin ice arrays. This is a first step towards realization of artificial spin ices as conceived

in model C, considering some freedom in the selection of its parameters.

Acknowledgments

The authors thank CNPq, FAPEMIG and CAPES (Brazilian agencies) for financial support; GMW gratefully acknowledges the hospitality and support of the Department of Physics at Universidade Federal de Viçosa where this work was carried out.

Appendix A: Langevin dynamics

The dynamics is investigated here using a Langevin approach^{29,30}. This includes a damping term and a rapidly fluctuating stochastic torque in the dynamics. The size of the stochastic torques is related to the temperature and the damping constant, such that the system tends towards thermal equilibrium for the chosen temperature. The approach also gives the dynamics at zero temperature but with the damping still included.

In practice, the dynamics is determined by *random magnetic fields*. This is an approach considered to be multiplicative noise^{31,32}, and most importantly, it gives the correct equilibrium dynamics. The dynamical equation for some selected unit dipole exposed to a deterministic field \vec{h} and a stochastic field \vec{h}_s is written in the dimensionless quantities as

$$\frac{d\hat{\mu}}{d\tau} = \hat{\mu} \times (\vec{h} + \vec{h}_s) - \alpha \hat{\mu} \times \left[(\hat{\mu} \times (\vec{h} + \vec{h}_s)) \right]. \quad (\text{A1})$$

The first term is the free motion and the second term is the Landau-Gilbert damping, with dimensionless damping constant α . For the stochastic fields to establish thermal equilibrium, their time correlations are determined by the fluctuation-dissipation (FD) theorem,

$$\langle h_s^i(\tau) h_s^j(\tau') \rangle = 2\alpha \mathcal{T} \delta_{ij} \delta(\tau - \tau'). \quad (\text{A2})$$

The indices i, j refer to any of the Cartesian coordinates. The dimensionless temperature \mathcal{T} is the thermal energy scaled by the energy unit,

$$\mathcal{T} = \frac{k_B T}{\varepsilon} = \frac{k_B T}{\mu \mu_0 M_s}. \quad (\text{A3})$$

The fluctuation-dissipation theorem indicates that the power in the thermal fluctuations is carried equivalently in the random magnetic fields. For reference, in physical units the FD relation is

$$\gamma \mu \langle B_s^i(t) B_s^j(t') \rangle = 2\alpha k_B T \delta_{ij} \delta(t - t'). \quad (\text{A4})$$

The Langevin equation in (A1) is a first-order differential equation where the noise is multiplicative. To discuss the solution method, it is simplest to let $y = y(\tau)$ be a vector that represents the entire set of spins, $y = \{\hat{\mu}_i(\tau)\}$.

Then symbolically y obeys a differential equation in the general form,

$$\frac{dy}{d\tau} = f[\tau, y(\tau)] + f_s[\tau, y(\tau)] \cdot h_s(\tau). \quad (\text{A5})$$

The function f represents the deterministic time derivative on the RHS of (A1) and the function f_s represents the stochastic part of the dynamics. Each is defined indirectly by comparing this with the Langevin equation. The fields f , f_s and h_s are vectors of $3N$ components, where N is the number of dipoles in the array.

Appendix B: Second order Heun integrator

An efficient method for integrating this magnetic dynamics type of equation forward in time is the second order Heun method^{29,30}. That is in the family of predictor-corrector schemes and is rather stable.

The predictor stage for the second order Heun algorithm is an Euler step, which is followed by a corrector stage that is equivalent to the trapezoid rule. Each involves moving forward in time over some time step $\Delta\tau$, with the needed results obtained by integrating Eq. A5 from an initial time τ_n to a final time $\tau_{n+1} = \tau_n + \Delta\tau$, during which the stochastic fields are acting. With notation $y_n \equiv y(\tau_n)$, the predictor stage produces an initial solution estimate \tilde{y}_{n+1} at the end of one time step,

$$\tilde{y}_{n+1} = y_n + f(\tau_n, y_n) \Delta\tau + f_s(\tau_n, y_n) \cdot (\sigma_s w_n). \quad (\text{B1})$$

The effect of the random fields is contained in the last term. The factor $\sigma_s w_n$ replaces the time-integral of the stochastic magnetic fields. For each site l of the array, there is a triple of unit variance, zero mean random numbers ($w_{ln}^x, w_{ln}^y, w_{ln}^z$) produced by a random number generator. The physical variance σ_s needed in the stochastic fields is defined by an equilibrium average over the time step. For an individual component at one site, that is

$$\sigma_s = \sqrt{\left\langle \left(\int_{\tau_n}^{\tau_{n+1}} d\tau h_s^x(\tau) \right)^2 \right\rangle} = \sqrt{2\alpha \mathcal{T} \Delta\tau}. \quad (\text{B2})$$

Thus, the integrated stochastic field components are replaced by random numbers of zero mean with the variance σ_s .

In the corrector stage, the points y_n and \tilde{y}_{n+1} are used to get better estimates of the slope of the solution. Their average effect becomes

$$y_{n+1} = y_n + \frac{1}{2} [f(\tau_n, y_n) + f(\tau_{n+1}, \tilde{y}_{n+1})] \Delta\tau \quad (\text{B3}) \\ + \frac{1}{2} [f_s(\tau_n, y_n) + f_s(\tau_{n+1}, \tilde{y}_{n+1})] \cdot (\sigma_s w_n).$$

It is important to note that the *same* random numbers w_n are used in this corrector stage as those applied in the predictor stage, for this individual time step.

The change in any spin over a time step, $\Delta\hat{\mu} = \int d\tau \frac{d}{d\tau} \hat{\mu}$, depends linearly on $\hbar\Delta\tau$ (deterministic) and linearly on $\int d\tau h_s(\tau)$ (stochastic). The stochastic contribution is replaced by random numbers of the correct variance,

$$\int_{\tau_n}^{\tau_n+\Delta\tau} d\tau h_s^x(\tau) \longrightarrow \sigma_s w_n^x. \quad (\text{B4})$$

Then the Euler predictor step is carried out by evaluating the combined deterministic plus stochastic field contributions, for an individual site, like

$$\tilde{\hat{\mu}} = \hat{\mu} + \Delta\hat{\mu}, \quad (\text{B5})$$

$$\Delta\hat{\mu} = \hat{\mu} \times [\vec{g} - \alpha(\hat{\mu} \times \vec{g})]. \quad (\text{B6})$$

The effective field that updates this site is a combination,

$$\vec{g} = \hbar[\tilde{\hat{\mu}}] \Delta\tau + \sigma_s \vec{w}. \quad (\text{B7})$$

The same type of combination applies in the trapezoid corrector stage, The updating field at the end of the time step is calculated using the *predicted position* together with the *same random fields*,

$$\vec{g} = \hbar[\tilde{\hat{\mu}}] \Delta\tau + \sigma_s \vec{w} \quad (\text{B8})$$

That leads to a different estimate for the spin change,

$$\tilde{\Delta}\hat{\mu} = \tilde{\hat{\mu}} \times [\vec{g} - \alpha(\tilde{\hat{\mu}} \times \vec{g})]. \quad (\text{B9})$$

Then the corrector stage gives the updated spin according to their average

$$\hat{\mu}(\tau + \Delta\tau) = \hat{\mu}(\tau) + \frac{1}{2} (\Delta\hat{\mu} + \tilde{\Delta}\hat{\mu}). \quad (\text{B10})$$

This algorithm does not ensure the conservation of spin length. Thus, the length of $\hat{\mu}$ can be rescaled to unity after the step.

The integration requires a sequence of quasi-random numbers (the \vec{w}_n stochastic fields) with a long period. We have used the generator `mzran13` due to Marsaglia and Zaman³³, implemented in the C-language for long integers. This generator is very simple and fast and has a period of about 2^{125} .

Appendix C: Dipole fields on an ice lattice

The calculation of the dipole term in the local magnetic field, (14), consumes most of the calculational effort. We consider a system with open boundaries. There are $N(N-1)/2$ dipole field contributions to be found at any time.

One of the best ways to speed up the calculation of the dipole fields for larger systems is to write their calculation as a convolution of a Green's function with the source dipoles, and calculate that convolution in reciprocal space, transforming between real and reciprocal space with a fast Fourier transform (FFT)³⁴. We consider that the spin ice involves unit cells on a square lattice, where each cell has a two-atom basis. Our approach also would work for other ice lattices with a different basis. For the cell whose lower left corner is at position $\vec{r}_k = (x_k, y_k) = (m_k, n_k)a$, define the two dipoles present. On the "1" sublattice,

$$\vec{\mu}_1(\vec{r}_k) \text{ at } \vec{r}_{k1} = (x_k + \frac{1}{2}a, y_k), \quad (\text{C1})$$

and on the "2" sublattice,

$$\vec{\mu}_2(\vec{r}_k) \text{ at } \vec{r}_{k2} = (x_k, y_k + \frac{1}{2}a). \quad (\text{C2})$$

If there is an arbitrary source dipole $\vec{\mu}$ at the origin, then the dipolar field \vec{h}^d it creates at position $\vec{r} = (x, y, z)$, according to the first term in (14), is well-known,

$$\vec{h}^d(\vec{r}) = \frac{d}{r^5} \begin{pmatrix} 2x^2 - y^2 & 3xy & 0 \\ 3xy & 2y^2 - x^2 & 0 \\ 0 & 0 & -r^2 \end{pmatrix} \cdot \begin{pmatrix} \mu^x \\ \mu^y \\ \mu^z \end{pmatrix} \quad (\text{C3})$$

(with all distances measured in lattice constants). This can be used to get the field produced from either sublattice. Summing over source dipoles, the 3×3 matrix is a Green's operator $\tilde{G}(\vec{r})$ acting on the dipoles at discrete lattice sites. (Here the tilde is used only to indicate a 3×3 matrix quantity.) However, to account for the two-atom basis, the Green's matrix is expanded to have an extra pair of indices that refer to the sublattice, one for the field point (α) and one for the source point (β). The Green's matrix for the field produced at point $\vec{r}_{k\alpha}$ due to the source dipole at point $\vec{r}_{l\beta}$ is

$$\tilde{G}_{\alpha\beta}(\vec{r}_k, \vec{r}_l) \equiv \frac{d}{|\vec{r}_{k\alpha} - \vec{r}_{l\beta}|^5} \begin{pmatrix} 2(x_{k\alpha} - x_{l\beta})^2 - (y_{k\alpha} - y_{l\beta})^2 & 3(x_{k\alpha} - x_{l\beta})(y_{k\alpha} - y_{l\beta}) & 0 \\ 3(x_{k\alpha} - x_{l\beta})(y_{k\alpha} - y_{l\beta}) & 2(y_{k\alpha} - y_{l\beta})^2 - (x_{k\alpha} - x_{l\beta})^2 & 0 \\ 0 & 0 & -|\vec{r}_{k\alpha} - \vec{r}_{l\beta}|^2 \end{pmatrix}. \quad (\text{C4})$$

It is important to keep in mind that $\tilde{G}_{\alpha\beta}$ actually depends only on the differences of the unit cell positions, $\vec{r}_{kl} \equiv \vec{r}_k - \vec{r}_l$. Now the dipole field on the α sublattice,

for the cell at \vec{r}_k , is given by a discrete convolution

$$\vec{h}_\alpha^d(\vec{r}_k) = \sum_{l=1}^{N_c} \sum_{\beta=1}^2 \tilde{G}_{\alpha\beta}(\vec{r}_k, \vec{r}_l) \cdot \vec{\mu}_\beta(\vec{r}_l). \quad (\text{C5})$$

Using fairly obvious notation, $\vec{\mu}_\beta(\vec{r}_l)$ is the dipole on the β sublattice for the unit cell at \vec{r}_l . The dot operation represents the matrix multiplication, i.e., an implicit sum over the Cartesian components of $\vec{G}_{\alpha\beta}$ and $\vec{\mu}_\beta$. Written this way, the same formula could apply to other lattices of interest, such as honeycomb, Kagomé, etc. Note that even at $\vec{r}_k - \vec{r}_l = 0$, there are contributions that must be included, corresponding to the interactions between the sublattices within an individual unit cell. For a specific example using the square ice sites, one can see that one particular interaction involving the two different sublattices ($\alpha = 1, \beta = 2$) has a Cartesian element,

$$G_{12}^{xx}(\vec{r}_k, \vec{r}_l) = d \frac{2(x_k - x_l + \frac{a}{2})^2 - (y_k - y_l - \frac{a}{2})^2}{[(x_k - x_l + \frac{a}{2})^2 + (y_k - y_l - \frac{a}{2})^2]^{5/2}} \quad (\text{C6})$$

This is nonzero when $\vec{r}_k = \vec{r}_l$. Also, the element $G_{21}^{xx}(\vec{r}_k, \vec{r}_l)$ with source and observer sublattices interchanged can be obtained by changing the sign of a ; they are not the same. A similar term with source and observer on the *same* sublattice is

$$G_{11}^{xx}(\vec{r}_k, \vec{r}_l) = d \frac{2(x_k - x_l)^2 - (y_k - y_l)^2}{[(x_k - x_l)^2 + (y_k - y_l)^2]^{5/2}} \quad (\text{C7})$$

This is equal to $G_{22}^{xx}(\vec{r}_k, \vec{r}_l)$. It is divergent at $\vec{r}_k = \vec{r}_l$, however, that is a self-interaction that must be excluded by definition.

$\vec{G}_{\alpha\beta}$ depends only on the displacements, $\vec{r}_{kl} \equiv \vec{r}_k - \vec{r}_l$, which form another square lattice. Then one can find its Fourier transform, using a fast Fourier transform (FFT), setting the arbitrary source point to the origin. The Fourier transform of $\vec{\mu}_\beta$ is also determined. The convolution in real space becomes a simple product of $\vec{G}_{\alpha\beta}$ and $\vec{\mu}_\beta$ in Fourier space, which can then be transformed back to real space by an inverse FFT to obtain \vec{h}^d . Although there is considerable overhead, for larger systems the speedup is tremendous ($N \ln N$ operations) when compared to doing the N sums with N terms to get the local dipole fields.

To apply the simplest FFT method, the size of the grid of primitive cells must be $2^{N_x} \times 2^{N_y}$ with integers

N_x and N_y . To avoid the wraparound problem, so that the system being simulated is really a single copy of the desired $L_x \times L_y$ size, one needs to choose N_x and N_y large enough so that $2^{N_x} > 2L_x$, and $2^{N_y} > 2L_y$. This ensures that the periodic copies of the system, inherent in the application of the Fourier transform, do not “see” or interfere with each other in the convolution.

There are some symmetries that reduce the calculational overhead. Displacements only on the 1-sublattice or only on the 2-sublattice are the same, so for any of its Cartesian components,

$$\vec{G}_{11} = \vec{G}_{22} . \quad (\text{C8})$$

Also, the matrix is symmetric in the Cartesian indices, for any sublattice indices,

$$G_{\alpha\beta}^{xy} = G_{\alpha\beta}^{yx} . \quad (\text{C9})$$

Furthermore, the interactions with both source and observer on the same sublattice are symmetrical in their interchange,

$$\vec{G}_{11}(\vec{r}_{kl}) = \vec{G}_{11}(\vec{r}_{lk}) = \vec{G}_{22}(\vec{r}_{kl}) = \vec{G}_{22}(\vec{r}_{lk}) . \quad (\text{C10})$$

The Fourier transforms of $G_{\alpha\alpha}$ are pure real, leading to some reduction in the computations needed. However, there is no symmetry between different sublattices on different unit cells, so $\vec{G}_{12}(\vec{r}_{kl}) \neq \vec{G}_{21}(\vec{r}_{kl})$, see the discussion after Eq. (C6). There are no self-interactions within a cell, so we do define $\vec{G}_{11}(0) = \vec{G}_{22}(0) = 0$. The interactions between sublattices on the same cell depend only on squared displacements, so $\vec{G}_{12}(0) = \vec{G}_{21}(0) \neq 0$. For $\vec{r}_{kl} \neq 0$, these symmetries result in 12 independent elements in $\vec{G}(\vec{r}_{kl})$ (each of \vec{G}_{11} , \vec{G}_{12} , and \vec{G}_{21} have 4 independent elements), in contrast to the 4 independent elements needed for a single sublattice, see the matrix in Eq. (C3).

References

-
- * Electronic address: wysin@phys.ksu.edu;
URL: <http://www.phys.ksu.edu/personal/wysin>
- † Electronic address: winder@ufv.br;
URL: <https://sites.google.com/site/wamouramelo/>
- ‡ Electronic address: lucasmol@ufv.br
- § Electronic address: apereira@ufv.br.;
URL: <https://sites.google.com/site/quantumafra/home>
- ¹ P.W. Anderson, Phys. Rev. **102**, 1008 (1956).
- ² L. Balents, Nature **464**, 199 (2010).
- ³ R. Moessner and A.R. Ramirez, Phys. Today **59**, 24 (2006).
- ⁴ C. Castelnovo, R. Moessner, and S.L. Sondhi, Nature **451**, 42 (2008).
- ⁵ I.A. Ryzhkin, JETP **101**, 481 (2005).
- ⁶ R.F. Wang, C. Nisoli, R.S. Freitas, J. Li, W. McConville, B.J. Cooley, M.S. Lund, N. Samarth, C. Leighton, V.H. Crespi and P. Schiffer, Nature **439**, 303 (2006).
- ⁷ J. Li, X. Ke, S. Zhang, D. Garand, C. Nisoli P. Lammert, V.H. Crespi, and P. Schiffer, Phys. Rev. B **81**, 092406 (2010).
- ⁸ S. Ladak, D.E. Read, G.K. Perkins, L.F. Cohen, and W.R. Brandford, Nature Phys. **6**, 359 (2010).
- ⁹ E. Mengotti, L.J. Heyderman, A.F. Rodriguez, F. Nolting, R.V. Hügli, and H-B Braun, Nature Phys. **7**, 68 (2011).
- ¹⁰ L.A.S. Mól, A.R. Pereira, and W.A. Moura-Melo, Phys.

- Rev. B **85**, 184410 (2012).
- ¹¹ C. J. Olson Reichhardt, A. Libsal and C. Reichhardt, New J. Phys. **14** 025006 (2012).
 - ¹² Z. Budrikis, K. L. Livesey, J. P. Morgan, J. Akerman, A. Stein, S. Langridge, C. H. Marrows and R. L. Stamps, New J. Phys. **14**, 035014 (2012).
 - ¹³ R. C. Silva, R. J. C. Lopes, L. A. S. Mól, W. A. Moura-Melo, G. M. Wysin and A. R. Pereira Phys. Rev. B **87**, 014414 (2013).
 - ¹⁴ F. S. Nascimento, L. A. S. Mól, W. A. Moura-Melo and A. R. Pereira, New J. Phys. **14**, 115019 (2012).
 - ¹⁵ J.P. Morgan, A. Stein, S. Langridge, and C. Marrows, Nature Phys. **7**, 75 (2011).
 - ¹⁶ L.A.S. Mól, R.L. Silva, R.C. Silva, A.R. Pereira, W.A. Moura-Melo, and B.V. Costa, J. Appl. Phys. **106**, 063913 (2009).
 - ¹⁷ L.A.S. Mól, W.A. Moura-Melo, and A.R. Pereira, Phys. Rev. B **82**, 054434 (2010).
 - ¹⁸ G. Möller and R. Moessner, Phys. Rev. B **80**, 140409(R) (2009).
 - ¹⁹ Y. Nambu, Phys. Rev. D **10**, 4262 (1974).
 - ²⁰ C. Nisoli, J. Li, X. Ke, D. Garandi, P. Schiffer, and V.H. Crespi, Phys. Rev. Lett. **105**, 047205 (2010).
 - ²¹ V. Kapaklis, U. B. Arnalds, A. Harman-Clarke, E. Th. Papaioannou, M. Karimipour, P. Korelis, A. Taroni P. C. W. Holdsworth, S. T. Bramwell, and B. Hjörvarsson, New J. Phys. **14**, 035009 (2012).
 - ²² R.C. Silva, F.S. Nascimento, L.A. S. Mól, W.A. Moura-Melo, and A.R. Pereira, New J. Phys. **14**, 015008 (2012).
 - ²³ G.M. Wysin, W.A. Moura-Melo, L.A.S. Mól and A.R. Periera, J. Phys.: Condens. Matter **24** 296001 (2012).
 - ²⁴ Zung-Hang Wei, Mei-Feng Lai, Ching-Ray Chang, N.A. Usov, J.C. Wu and Jun-Yang Lai, J. Mag. Magn. Mater. **272-276**, e563 (2004).
 - ²⁵ Z. Budrikis, P. Politi, and R.L. Stamps, Phys. Rev. Lett. **105**, 017201 (2010).
 - ²⁶ Z. Budrikis, P. Politi, and R.L. Stamps, Phys. Rev. Lett. **107**, 217204 (2011).
 - ²⁷ Z. Budrikis, J. P. Morgan, J. Arkeman, A. Stein, P. Politi, S. Langridge, C.H. Marrows, and R.L. Stamps, Phys. Rev. Lett. **109**, 037203 (2012).
 - ²⁸ D. Levis and L. F. Cugliandolo, EPL (Europhysics Letters) **97**, 30002 (2012).
 - ²⁹ J.L. García-Palacios and F.J. Lázaro, Phys. Rev. B **58**, 14937 (1998).
 - ³⁰ U. Nowak, in *Annual Reviews of Computational Physics IX*, p. 105, edited by D. Stauffer (World Scientific, Singapore, 2000).
 - ³¹ T. Kampeter, F.G. Mertens, E. Moro, A. Sánchez and A.R. Bishop, Phys. Rev. B **59**, 11349 (1999).
 - ³² Ph. Depondt and F.G. Mertens, J. Phys.: Condens. Matter **21**, 336005 (2009).
 - ³³ G. Marsaglia and A. Zaman, Computers in Physics **8**, No. 1, 117, (1994).
 - ³⁴ J. Sasaki and F. Matsubara *J. Phys. Soc. Japan*, **66**, 2138 (1997).